Investigation of the Validity of the Image Model for the Analysis of Spherical Wave Reflection

*Jin-Sung Suh and *Wan-Sup Cheung

Abstract

The validity of the image model is investigated both analytically and experimentally in a half space with an infinite single reflecting surface present. This paper exploits the Sommerfeld integral that represents the exact solution for the reflected field in the half space. The solution is shown to be obtained by direct numerical integration which yields more accurate and stable results. The predicted results from the image model are compared to those from the direct numerical integration of the Sommerfeld integral. It is also experimentally demonstrated that the image model gives acceptably accurate results. It is of significance that this paper reveals analytical and experimental validation of using the image model except near-grazing incidence.

I. Introduction

The reflection of a spherical wave on an infinite plane boundary in a half space is usually explained by putting an image source at the mirror-image position of the real source with respect to the infinite plane boundary and by using the complex reflection coefficient of the plane boundary. It has been the basic theory which is used by the image model. However, this is true only when the reflective properties of the plane boundary is independent of the angle of incidence. It implies that the image model is also an approximate solution. For instance, the image model can be used to measure the incident-angle dependent reflective properties of plane surfaces[1]. Therefore it is necessary to examine how close the basic theory of the image model is to an exact solution and in what situation this can be used to represent reflections with reasonable accuracy.

The exact solution to the reflected field in a half space is given by the "Sommerfeld integral", which was formulated by decomposing a spherical wave radiated from a monopole source into an infinite number of plane waves [2]. In order to solve the Sommerfeld integral several assumptions and approximations have been made by using such as the complementary error function[3], the saddle point method[4], the steepest descent method[5], and the series expansion method[6]. In this work the Sommerfeld integral is shown to be solved by direct numerical integration under the local reaction assumption. This enables the calculation of the accuracy of the image model.

* Acoustics/Vibration Group, KRISS

Manuscript Received : July 16, 1998.

It is shown that the exact reflected field, in most cases, can be replaced by the contribution made by an image source with good accuracy except near-grazing incidence. Furthermore, experimental work in addition to this fact is inevitable to examine the validity of the image model.

II. Comparison Between the Analytical Solution and the Image Model

The complex acoustic pressure $p(x, y, z)$ at the receiver position in Fig. 1, when the source strength(volume acceleration) is unity, is given by

$$p(x, y, z) = \frac{\rho_0 e^{-jkr_0}}{4\pi r_0} + p_{refl} \tag{1}$$

where p_{refl} is the reflected wave field, k is the wave number of the spherical wave radiated from the monopole source, and ρ_0 is the ambient density of air. Since the wavefront of a spherical wave is incompatible with a plane boundary, it is necessary to decompose a spherical wave into an infinite number of plane waves. By decomposing a spherical wave into an infinite number of plane waves p_{refl} can be expressed by[7]

$$p_{refl} = -\frac{j\rho_0 k}{4\pi} \int_{r_e} J_0(kr\sin\theta) e^{-jk(z+z_0)\cos\theta} R(\theta) \sin\theta d\theta \tag{2}$$

where $R(\theta)$ is the complex reflection coefficient of the infinite plane boundary which depends upon the angle of incidence, θ, and $J_0(kr\sin\theta)$ is the Bessel function of zeroth order.
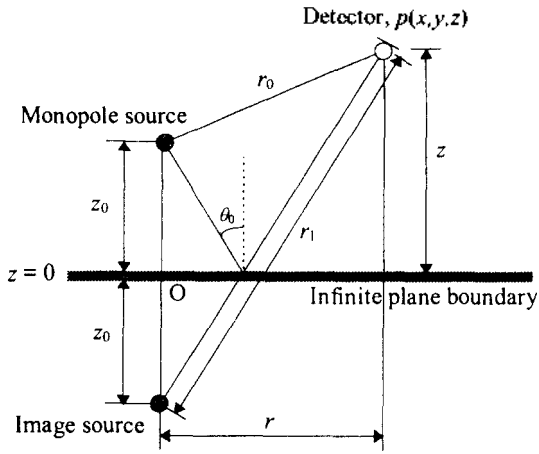
Figure 1. Configuration of source and detector in a half space.
O is the origin of the coordinate system.

Then Eq. (2) can be computed by numerical integration technique[8]. It can be easily demonstrated that, except grazing incidence, Eq. (2) converges rapidly. The numerical integration technique used in this work is the Trapezoidal rule. The magnitude of the constant step $\triangle \theta$ replacing $d\theta$ in Eq. (2) should be made as small as possible for good accuracy. A value of 10^{5} radians was chosen for $\triangle \theta$ in this work. In Appendix A, the underlying principles of the numerical integration used in this paper are presented and a specific result is shown which demonstrates the convergence of the integral.

The reflection coefficient $R(\theta)$ of a locally reacting plane boundary, when a plane wave is incident upon it, can be expressed as

$$R(\theta) = \frac{\xi \cos \theta - 1}{\xi \cos \theta + 1} \qquad (3)$$

where ξ is the specific acoustic impedance of the infinite plane boundary normalized by the characteristic impedance $\rho_0 c$ of air, and c is the speed of sound. In this paper, it is assumed that all the acoustic materials are locally reacting. In most cases, except the near-grazing incidence, p_{refl} can be replaced with good approximation by

$$p_{image} = \frac{\rho_0 e^{jkr_1}}{4\pi r_1} R(\theta_0) \qquad (4)$$

This is the contribution to the total field made by the image source as illustrated in Fig. 1. The percentage error(%) between p_{refl} and p_{image} can be defined as

$$\frac{|p_{refl} - p_{image}|}{|p_{refl}|} \times 100(\%)$$

In Fig. 2.1, 2.2, and 2.3, this is plotted against the angle of incidence θ_0 for three different values of ξ when r is 2λ, 5λ, 10λ, respectively where λ is the wavelength. The ξ's are tabulated in Table 1 together with the corresponding diffuse absorption coefficient, α_d, when local reaction is assumed[9]. It should be noted that the results illustrated in Fig. 2.1, 2.2, and 2.3 are independent of frequency since the values of r, r_1, z_0, and z were given in terms of λ.

The results demonstrate that the degree of accuracy achieved by using Eq. (4) to define the reflected field is most sensitive to the angle of incidence θ_0. When θ_0 is smaller than $60°$, the true reflected field can be replaced by Eq. (4) with good accuracy provided that the detector position is many wavelengths from the source. In general, Eq. (4) is a good approximation to the reflected field except for grazing incidence sound or surfaces of high absorption coefficient when the source-receiver distance is less than or equal to a few wavelengths. It is worthwhile to note the trends of the error curves shown in Fig. 2.1, 2.2, and 2.3. Specifically when the angle of incidence is greater that $65°$, the image model produces more accurate predictions for the case when the plane boundary has an absorption coefficient of 0.71 than for the cases when it has a value either 0.21 or 0.41.

Table 1 The acoustic properties of the infinite plane boundary.
(ξ: Specific acoustic impedance, α_d: diffuse absorption coefficient)

	ξ	α_d
curve 1	5.00 $j11.00$	0.21
curve 2	1.00 $j2.83$	0.41
curve 3	0.59 + $j0.57$	0.71

Figure 2.1. The percentage (%) error between p_{refl} and p_{image}. The angle of incidence denotes θ_0 in Fig. 1. r is 2λ.
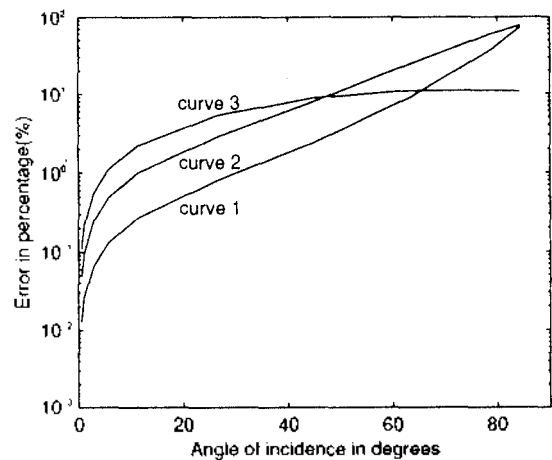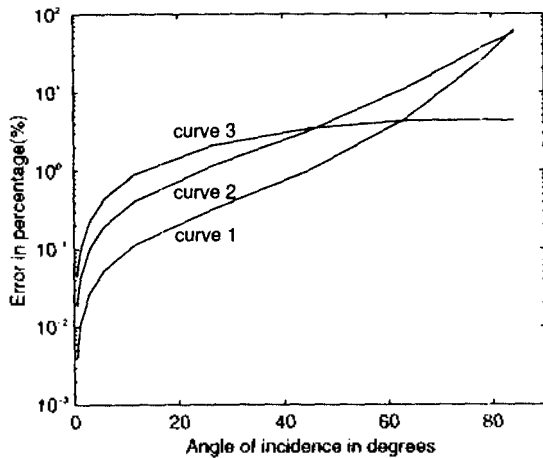
Figure 2.2. The percentage (%) error between p_{refl} and p_{image}. The angle of incidence denotes θ_0 in Fig. 1. r is 5λ.

Figure 2.3. The percentage (%) error between p_{refl} and p_{image}. The angle of incidence denotes θ_0 in Fig. 1. r is 10λ.
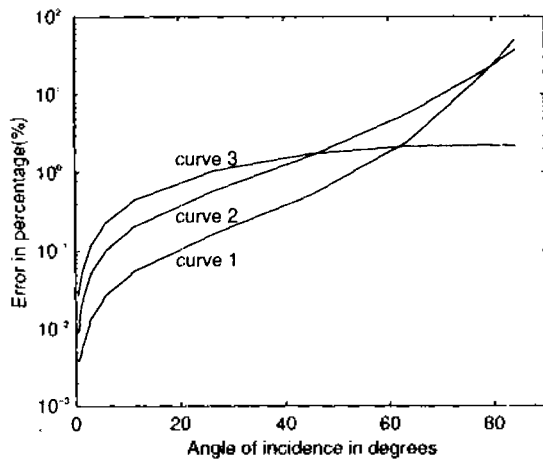
III. Comparision of the Acoustical Frequency Response Functions Between Measurement and the Image Model

The measurement set-up is drawn in Fig. 3. A 5cm-thick plastic foam, which is an open cell type, is used to cover a 5cm-thick high-density fibre-board. The intention was to simulate a rigid-backing condition. The mon-opole source used in the measurement is shown in Fig. 4. For the source and microphone positions shown in Fig. 3 the angle of incidence is about 27°. According to the error curves plotted in Fig. 2.1, 2.2, and 2.3, the expected error of the image model will be less than 5% when the diffuse absorption coeffcient of the plastic foam
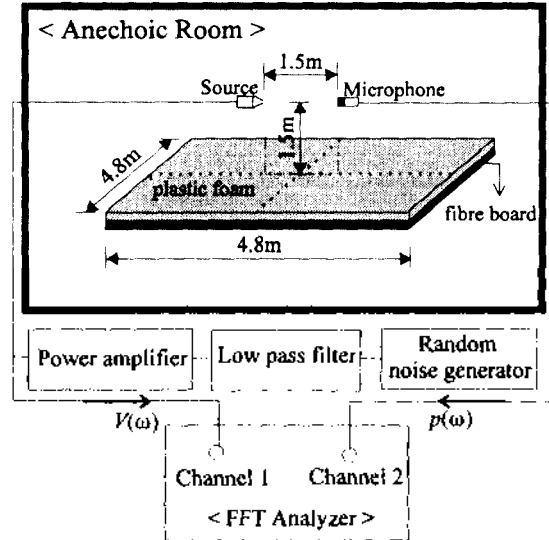
has a value less than 0.71.

Figure 3. Measurement set-up. $p(\omega)$: is the pressure signal measured at the microphone. $V(\omega)$: The acoustic source driving signal
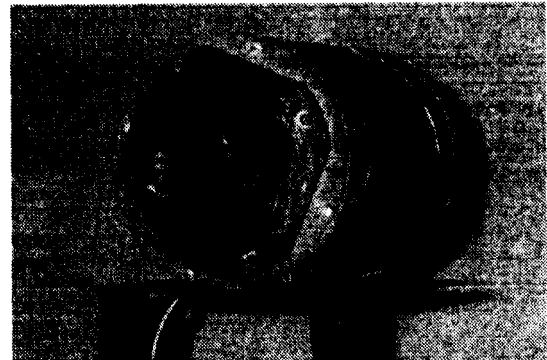

Figure 4. Monopole source used in the measurement. The opening diameter of the horn is 28mm. A loudspeaker unit 15cm in diameter is fixed between the horn and the cylindrical body.

Its directivity will depend upon the polar angle measured from the central axis. Let us denote the directivity of the source as $D(\omega, \theta^\circ)$ when the angular frequency is ω and the polar angle is θ°. As an illustration $D(\omega, 63^\circ)/D(\omega, 0^\circ)$ was measured in an anechoic room, and is plotted in Fig. 5. This source shows good omnidirection-ality over the whole range of polar angles on the frquency range of 80 Hz to 800 Hz.

The frequency response function between the pressure and the output drive voltage of the power amplifier in Fig. 3, $p(\omega)/V(\omega)$, is plotted in Fig. 6. In order to obtain the acoustical frequency response function which is the
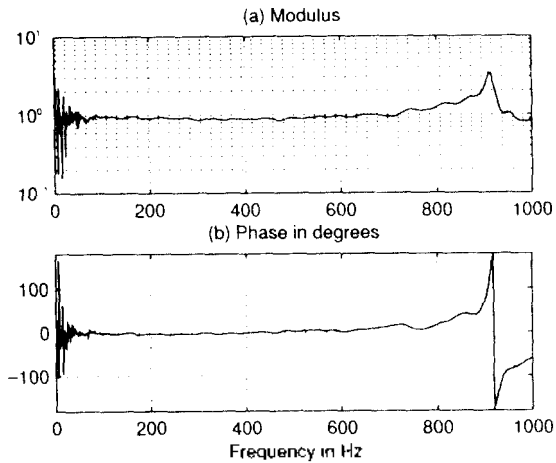
(a) Modulus

(b) Phase in degrees

Figure 5. Relative directivity $D(\omega, 63^\circ)/D(\omega, 0^\circ)$ of the source shown in Fig. 4.

pressure response per unit source strength, a source calibration was carried out in an anechoic chamber using the same measurement set-up that is shown in Fig. 3. In this paper, volume acceleration is chosen to be the source strength. Like the previous measurement, $p(\omega)/V(\omega)$ was measured. This is shown in Fig. 7. The volume acceleration per unit output drive voltage of the power amplifier, $\dot{q}(\omega)/V(\omega)$, can be computed from

$$\frac{\dot{q}(\omega)}{V(\omega)} = \frac{4\pi r_{cal} \, exp(jkr_{cal})}{\rho_0} \cdot \frac{p(\omega)}{V(\omega)} \quad (5)$$

where $\dot{q}(\omega)$ denotes the time derivative of the volume velocity, and r_{cal} is the distance between the source and the microphone. In this measurement, r_{cal} was 2.3m. In order to produce the simulated frequency response function
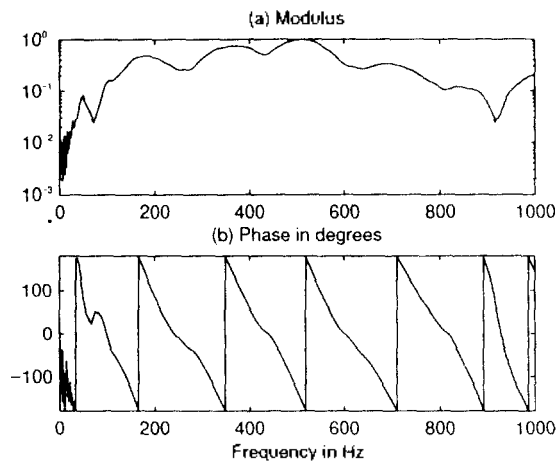
(a) Modulus

(b) Phase in degrees

Figure 6. The frequency response function between the pressure and the output drive voltage of the power amplifier for the single surface measurement.(Refer to Fig. 3.)
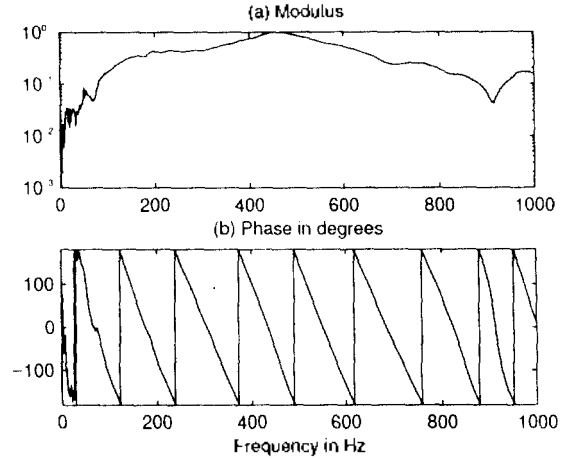
(a) Modulus

(b) Phase in degrees

Figure 7. The frequency response function between the pressure and the output drive voltage of the power amplifier in an anechoic chamber.

from the image model, the normal specific impedance of the plastic foam, ξ, was measured by an impedance tube test with a rigid backing condition. The results are plotted in Fig. 8. This enabled $R(\theta_0)$ to be calculated from Eq. (3).The acoustical frequency response function can be obtained by dividing the frequency response function shown in Fig. 6 by Eq. (5). This is shown in Fig. 9 together with that simulated by the image model. Excellent agreement is shown.

IV. Comparision of the Pressure Impulse Responses Between Measurement and Image Model

It is also useful to compare the time domain responses. The impulse response functions are defined for an omni-
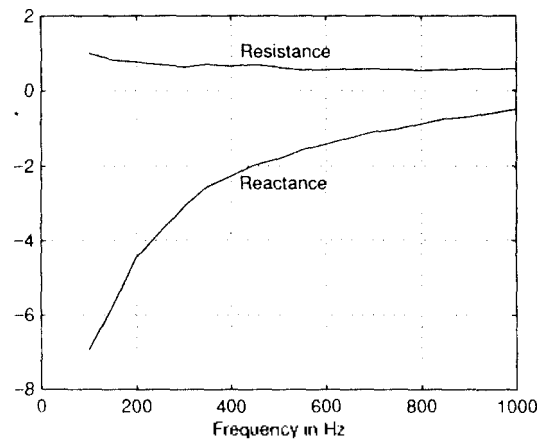
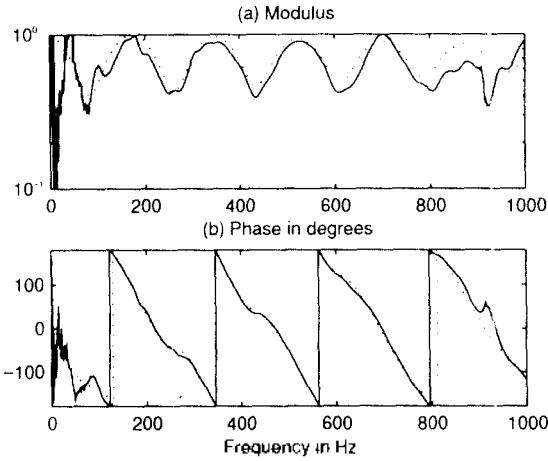Figure 8. Normal specific acoustic impedance of the plastic foam.

(a) Modulus

(b) Phase in degrees

Frequency in Hz

Figure 9. The acoustical frequency response functions obtained from the measurement and the phase image model. Measurement: ———, Phase image model: · ·······

directional source. Also real acoustic sources are reasonably omnidirectional only within limited frequency bandwidth. Therefore a suitable source strength signal defined within this bandwidth should be used. Here, we illustrate the importance of the choice of this limited bandwidth signal.

For any band limited time signal, the product of the time width $\triangle t$ and its frequency bandwidth $\triangle \omega$ (or $\triangle f$) is always subject to the restriction of the "Uncertainty principle" which states that

$$\triangle t \triangle \omega \geq \pi \quad \text{or} \quad \triangle t \triangle f \geq 0.5 \quad (6)$$

where ω is in radians/sec and f is in cycles/sec. We illustrate the importance of using a signal whose value of $\triangle t$ is as small as possible for a given $\triangle \omega$ by presenting the results of using two different signals. The first source strength signal to be used is $\Psi_1(t)$ given by[10]

$$\Psi_1(t) = \frac{\sin \frac{1}{2} (\triangle \omega) t}{\frac{1}{2} (\triangle \omega) t} \cos(\omega_0 t) \quad (7)$$

where the product $\triangle t \triangle \omega$ takes the value of 2π and ω_0 is the centre frequency of the band. Thus $\triangle t$ is twice the minimum value possible for the given value of $\triangle \omega$. Its Fourier Transform $\psi_1(\omega)$ is a square spectrum given by

$$\psi_1(\omega) = \begin{cases} \dfrac{1}{\triangle \omega} & \text{for} \quad \omega_0 - \dfrac{\triangle \omega}{2} \leq \omega \leq \omega_0 + \dfrac{\triangle \omega}{2} \\ 0 & \text{for} \quad \omega_0 - \dfrac{\triangle \omega}{2} > \omega > \omega_0 + \dfrac{\triangle \omega}{2} \end{cases} \quad (8)$$

The second source strength signal is a Gabor pulse, $\Psi_2(t)$, given by

$$\Psi_2(t) = e^{-a^2 t^2} \cos(\omega_0 t) \quad (9)$$

$\Psi_2(t)$ is the real part of the Gabor elementary signal, $g(t)$, given by[11,12]

$$g(t) = e^{-a^2 t^2} e^{j\omega_0 t} \quad (10)$$

where the product $\triangle t \triangle \omega$ takes the minimum value of π. For $g(t)$, the constant a is related to $\triangle t$, $\triangle \omega$ by

$$\triangle t = \sqrt{\frac{\pi}{2}} \frac{1}{a} \quad , \quad \triangle \omega = \sqrt{2\pi} \, a \quad (11)$$

For $\Psi_2(t)$, however, the product $\triangle t \triangle \omega$ becomes approximately π. Its Fourier Transform $\psi_2(\omega)$ is given by

$$\psi_2(\omega) = \frac{1}{2} \frac{\sqrt{\pi}}{a} \left[e^{-\pi^2 \frac{(\omega + \omega_0)^2}{4a^2}} + e^{-\pi^2 \frac{(\omega - \omega_0)^2}{4a^2}} \right] \quad (12)$$

For the single surface reflection experiment described above, Fig. 10 shows $\Psi_1(t)$ and $\psi_1(f)$ with $\triangle t = 1/300$ sec, $\triangle f = 300$ Hz, and $f_0 = 500$ Hz. The pressure impulse responses due to $\Psi_1(t)$ are compared in Fig. 11. Fig. 12 shows $\Psi_2(t)$ and $\psi_2(f)$ with $\triangle t \cong 1/600$ sec, $\triangle f \cong 300$ Hz, $f_0 = 500$ Hz. The pressure impulse responses due to $\Psi_2(t)$ are compared in Fig. 13. These

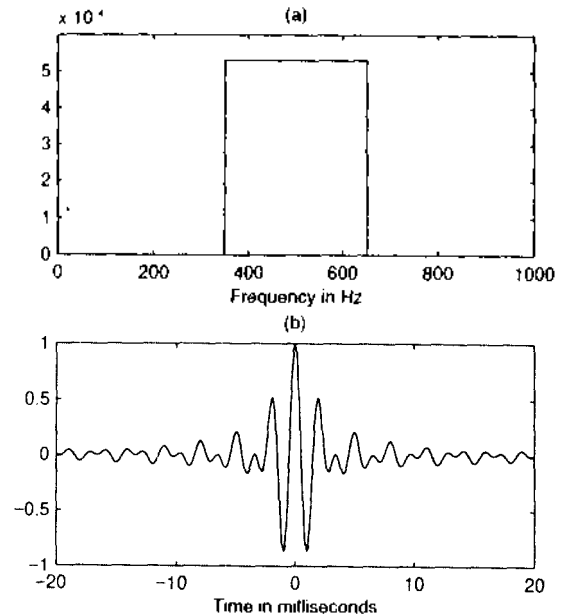x 10⁴ (a)

Frequency in Hz

(b)

Time in milliseconds

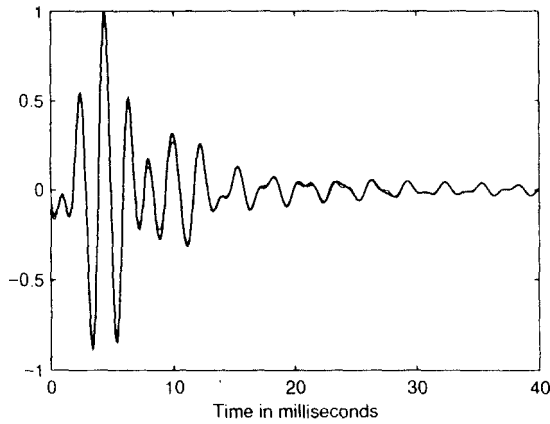Figure 10. Source strength signal ; (a) $\psi_1(f)$, and (b) $\Psi_1(t)$.

Figure 11. Pressure impulse responses due to $\Psi_1(t)$.
. Measurement: Thick solid line,
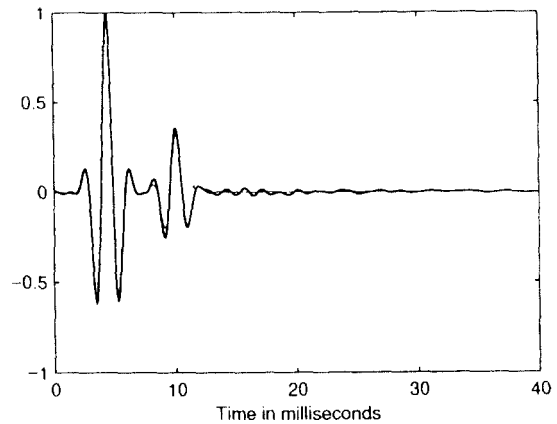Phase image model: Thin solid line

results were computed by taking the inverse Fourier trans-
form of the product of the acoustical frequency response
function and the Fourier transform of the source strength
signal.

For both of the input signals the image model predicts
the measured impulse responses with good accuracy even
though the incident angle dependent reflection coefficient
was deduced from a local reaction assumption. A Gabor
pulse has the advantage over other types of signal that
its time duration is the shortest possible for a given fr-
equency bandwidth. Fig. 13 in particular shows how well
the direct and first reflected pulses are resolved when the
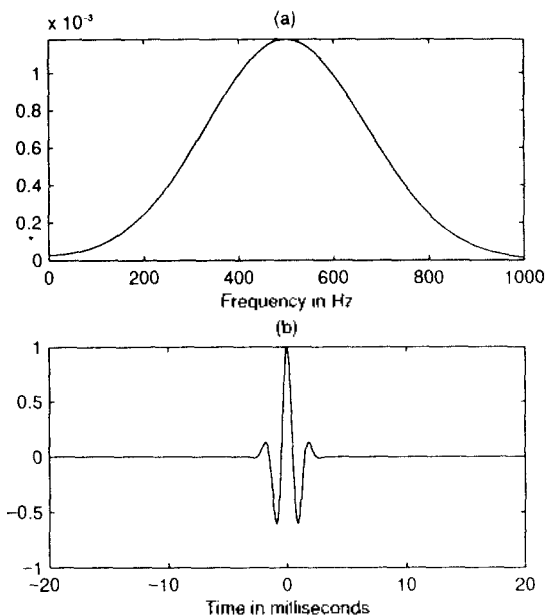source strength time history is a Gabor pulse.

Figure 12. Source strength signal ; (a) $\phi_2(f)$, and (b) $\Psi_2(t)$.

Figure 13. Pressure impulse responses due to $\Psi_2(t)$.
Measurement: Thick solid line,
Phase image model: Thin solid line

V. Conclusion

The validity of using the image model was obviously
demonstrated by the theoretical analysis and measurement
performed in a single reflecting surface environment. It
was shown that the accuracy of the image model is most
sensitive to the angle of incidence. Except for near-grazing
incidence, the image model was shown to approximate the
reflected field with good accuracy. The Sommerfeld inte-
gral representing the exact reflected field was solved by
direct numerical integration, which provides a good guide-
line for testing the validity of the various models for
computing the reflected field in the half space. The re-
flected field predicted by the image model was in good
agreement with that measured. By introducing a Gabor
pulse as a source strength signal, the direct wave and the
first-reflected wave could be almost completely resolved
for both measurement and the image model.

Acknowledgments

Reference

1. A. J. Cramond, and C. G. Don, "Reflection of impulses as
a method of determining acoustic impedance," J. Acoust.
Soc. Am. Vol. 75, pp. 382-389, 1984.

2. A. Sommerfeld, "Über die Ausbreitung der Wellen in der
Drahtlosen Telegraphie," Ann. Phys. Vol. 28, pp. 665-736,
1909.

3. U. Ingard, "On the Reflection of a Spherical Sound Wave
from an Infinite Plane," J. Acoust. Soc. Am. Vol. 23, pp.
329-335, 1951.

4. T. Kawai, T. Hidaka, and T. Nakajima, "Sound Propagation Above an Impedance Boundary," *J. Sound Vib.* Vol 83, pp. 125-138, 1982.

5. K. Attenborough, S. I. Hayek, and J. M. Lawther, "Propagation of sound above a porous half-space," *J. Acoust. Soc. Am.* Vol. 68, pp. 1493-1501, 1985.

6. D. Habault, "Diffraction of a Spherical Wave by Different Models of Ground: Approximate Formulas," *J. Sound Vib.* Vol. 68, pp. 413-425, 1980.

7. L. M. Brekhovskikh, *Waves in Layered Media*, Second Edition, Academic Press, 1980.

8. S. Thomasson, "Reflection of waves from a point source by an impedance boundary," *J. Acoust. Soc. Am.* Vol. 59, pp. 780-785, 1976.

9. H. Kuttruff, *Room Acoustics*, Third Edition, Elsevier, Applied Science, 1991.

10. F. S. Crawford, *Waves*, Third Edition, Berkeley Physics Course-Vol. 3, Education Development Center, Inc., pp. 286-292, 1968.

11. D. Gabor, "Theory of Communication," *Journal of the IEEE*, London Vol. 93(III), pp. 429-457, 1946.

12. J. K. Hammond, and P. R. White, "The analysis of non-stationary signals using time-frequency methods," *J. Sound Vib.* Vol. 190, pp. 419-447, 1996.

Appendix A. Basic Theory for Numerical Integration of EQ. (2)

The integration contour Γ_θ can be divided into two paths. Path Γ_1 extends from 0 to $\pi/2$ on the real axis. Path Γ_2 extends from $\pi/2$ to $\pi/2 + j\infty$. This is illustrated in Fig. A.1. Eq. (2) is also known as the Sommerfeld Integral.
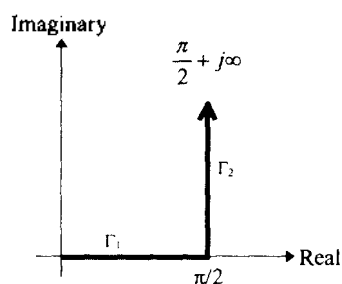

Figure A.1. Integration contour, $\Gamma_\theta (= \Gamma_1 + \Gamma_2)$, in the complex θ-plane.

The Sommerfeld Integral evaluated along path Γ_1, which will be denoted by $p_{refl.1}$, will be given by

$$p_{refl.1} = -\frac{j\rho_0 k}{4\pi} \int_0^{\pi/2} J_0(kr\sin a)\exp(-jk(z+z_s)\cos a)R(a)\sin a\, da \tag{A1}$$

where $R(a)$ is

$$R(a) = \frac{\xi\cos a - 1}{\xi\cos a + 1} \tag{A2}$$

By using the identity

$$\cos(\tfrac{\pi}{2}+j\beta) = \cos\tfrac{\pi}{2}\cosh\beta - j\sin\tfrac{\pi}{2}\sinh\beta = -j\sinh\beta$$
$$\sin(\tfrac{\pi}{2}+j\beta) = \sin\tfrac{\pi}{2}\cosh\beta + j\cos\tfrac{\pi}{2}\sinh\beta = \cosh\beta \tag{A3}$$

The Sommerfeld integral evaluated along path Γ_2, which will be denoted by $p_{refl.2}$, will be given by

$$p_{refl.2} = \frac{\rho_0 k}{4\pi} \int_0^\infty J_0(kr\cosh\beta)\frac{\cosh\beta}{\exp(ksinh\beta(z+z_s))}$$
$$R(\tfrac{\pi}{2}+j\beta)\,d\beta \tag{A4}$$

where $R(\tfrac{\pi}{2}+j\beta)$ is

$$R(\tfrac{\pi}{2}+j\beta) = \frac{j\xi\sinh\beta + 1}{j\xi\sinh\beta - 1} \tag{A5}$$

Thus the solution of the Sommerfeld integral is the sum of $p_{refl.1}$ and $p_{refl.2}$. $p_{refl.1}$ is a definite integral but $p_{refl.2}$ is an improper integral whose integration variable β extends from 0 to ∞. Except grazing incidence, it can be easily noticed that the integrand of Eq. (A.4) is a rapidly decaying function of β converging toward zero. Let us express the integrand of Eq. (A4) by $F(\beta)$. Then $p_{refl.2}$ can be expresseded by

$$p_{refl.2} = \frac{\rho_0 k}{4\pi} \int_0^1 F(\beta)\,d\beta + \frac{\rho_0 k}{4\pi} \int_1^2 F(\beta)\,d\beta$$
$$+ \frac{\rho_0 k}{4\pi} \int_2^3 F(\beta)\,d\beta + \cdots \tag{A6}$$

Let us denote each term in Eq. (A6) by A(0), A(1), A(2), A(4), ⋯. Then Eq. (A6) can be represented by

$$p_{refl.2} = A(0) + A(1) + A(2) + \cdots \tag{A7}$$

If the series A(0), A(1), A(2), ... is rapidly converging toward zero, then $p_{refl.2}$ can be computed. Actually they do converge except grazing incidence. The numerical technique used is the Trapezoidal rule. da and $d\beta$ in Eq. (A1) and (A4) will be replaced by $\triangle a$ and $\triangle \beta$, which

are constant steps on α and β axis, respectively. For good accuracy, $\wedge \alpha$ and $\wedge \beta$ should be made as small as possible. One example of the numerical integration was undertaken for the following configuration shown in Fig. A.2. Several values of $\wedge \alpha$ and $\wedge \beta$ were used in order to investigate the convergence of Eq. (A1) and (A4). The specific acoustic impedance ξ of the surface was assumed to be 5.00 $j11.00$ with local reaction assumed. The values of c and ρ_0 used are 344 m/sec and 1.21 kg/m^3.
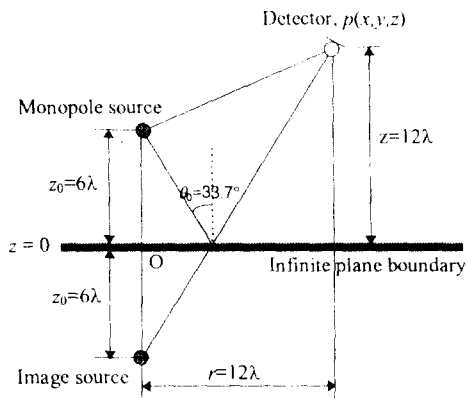

Figure A.2. Configuration of source and detector in a half space. O is the origin of the coordinate system.

The results are presented in Table A.1. It is evident that as $\wedge \alpha$ and $\triangle \beta$ become smaller, the Sommerfeld integral converges

▲Jin Sung Suh

Jin Sung Suh received the B.S. degree in mechanical design & production engineering from Seoul National University, Korea, in 1985, the M.S. and Ph.D. degrees in acoustics from the Institute of Sound and Vibration Research, the University of Southampton, U.K., in 1988 and 1998, respectively. From 1989 to 1992, he was a research engineer at the Technical Center of Daewoo Motor Co. Currently he is working at the Acoustics/Vibration Lab, Korea Research Institute of Standards and Science, Korea. His current research interests include room acoustic simulation and acoustic measurement techniques.

▲Wan-Sup Cheung

Wan-Sup Cheung received the B.S. and M.S. degrees in mechanical engineering from Hangyang University, Korea, in 1982 and 1984, respectively. His Ph.D. degree was awarded in signal processing and control from the Institute of Sound and Vibration Research, the University of Southampton, U.K., in 1993. Since 1984 he has been working for the Acoustics/Vibration Lab, Korea Research Institute of Standards and Science, Korea. His current research interests include human-related acoustics and vibration, specificially 3D Sound and vibration ride quality in transportation vehicles.

Table A.1. Comparison of the numerical integrations with different spacings of $\wedge \alpha$ and $\wedge \beta$.

	$p_{refl,1}$	$p_{refl,2}$	$p_{refl,1} = p_{refl,1} + p_{refl,2}$
$\triangle \alpha = \triangle \beta = 10^{-4}$	$-1.00323e-2 + j2.06514e-2$	$-2.48551e-3 - j3.00200e-4$	$-1.25178e-2 + j2.03512e-2$
$\triangle \alpha = \wedge \beta = 10^{-5}$	$-1.00323e-2 + j2.06514e-2$	$-2.48550e-3 - j3.00202e-4$	$-1.25178e-2 + j2.03512e-2$
$\wedge \alpha = \triangle \beta = 10^{-6}$	$-1.00323e-2 + j2.06514e-2$	$-2.48550e-3 - j3.00202e-4$	$-1.25178e-2 + j2.03512e-2$